Earth and Planetary Science Letters 465 (2017) 1–15

Contents lists available at ScienceDirect

Earth and Planetary Science Letters

www.elsevier.com/locate/epsl

Cooling history of the Gongga batholith: Implications for the Xianshuihe Fault and Miocene kinematics of SE Tibet

Yuan-Ze Zhang [a,1], Anne Replumaz [b,*], Philippe Hervé Leloup [c], Guo-Can Wang [a,d], Matthias Bernet [b], Peter van der Beek [b], Jean Louis Paquette [e], Marie-Luce Chevalier [f]

[a] Center for Global Tectonics, School of Earth Sciences, China University of Geosciences, Wuhan 430074, China
[b] ISTerre, Université Grenoble Alpes, CNRS, F-38400 Grenoble, France
[c] Laboratoire de géologie, Université Lyon 1, ENS de Lyon, CNRS, UMR 5276 LGL-TPE, F-69622, Villeurbanne, France
[d] State Key Laboratory of Geological Processes and Mineral Resources, China University of Geosciences, Wuhan 430074, China
[e] CNRS UMR 6524, Université Blaise Pascal, 63038 Clermont Ferrand CX, France
[f] Institute of Geology, Chinese Academy of Geological Sciences, Beijing 100037, China

ARTICLE INFO

Article history:
Received 5 September 2016
Received in revised form 13 January 2017
Accepted 14 February 2017
Available online xxxx
Editor: A. Yin

Keywords:
Tibetan Plateau
Gongga batholith
Xianshuihe fault
low-temperature thermochronology
continental tectonics
landscape evolution

ABSTRACT

Using thermochronological data and thermokinematic modeling, we constrain the timing of late Miocene exhumation of the northern portion of the Gongga batholith, located in Southeast Tibet along the Xianshuihe Fault (XF). We show that rapid exhumation started in the north of the Gongga batholith at ~9 Ma at a rate of ~1.85 km/Myr and slowed down since ~4 Ma. A magmatic pulse occurring during the early Pliocene (~4 Ma) has overprinted the rapid Miocene exhumation phase in some parts of the batholith, which record mainly early Pliocene post-magmatic cooling. Slow exhumation since ~4 Ma is consistent with the present-day lower relief observed in the centre of the batholith, which contrasts with the rugged high peaks located to the south. We propose that the northern segment of the XF, the Yalahe fault, which is not active at present, was active between 9 and 4 Ma, forming a restraining bend that focused exhumation south of it. Since ~4 Ma, the Selaha and the Zheduotang faults form the present-day restraining bend south of which the highest part of the massif is located, including the Gongga Shan that rises more than 3000 m above the mean elevation of the plateau. In the north of the batholith, similar peaks have been removed since the Miocene by local relief reduction at high elevations. Considering that the onset of motion along the XF is contemporaneous with the onset of rapid exhumation recorded along the Kangding transect at ~9 Ma and a total offset of ~62 km documented for the XF, the average slip rate of the XF is ~7 mm/yr since 9 Ma.

1. Introduction

The indentation of Asia by India has resulted in the build-up of the Earth's largest and highest orogenic plateau, the Tibetan Plateau. The eastern margin of the Tibetan Plateau has long been considered as a natural laboratory to test different models of plateau evolution (e.g. Clark et al., 2005a; Liu-Zeng et al., 2008; Wang et al., 2012). Thermochronological data provide key constraints on the timing and the rate of cooling to resolve controversies concerning the timing of regional surface uplift, exhumation and incision of the eastern Tibetan Plateau (e.g., Kirby et al., 2002; Clark et al., 2005b; Ouimet et al., 2010; Wang et al., 2012; Zhang et al., 2016). Among the most extensively studied target is the Gongga batholith, the emblematic Cenozoic batholith of Southeast Tibet, which has been exhumed during the Miocene–Pliocene (e.g., Roger et al., 1995; Xu and Kamp, 2000). This batholith hosts the highest peak on earth outside of the Himalayas, the Gongga (or Minya Konka) peak at 7556 m, which towers above the ~4000 m-high plateau, less than ~100 km away from the ~500 m-high Sichuan basin (Fig. 1). The Gongga batholith is located along the Xianshuihe Fault (XF), part of the Xianshuihe fault system running from the Ganzi fault to the north to the Zemuhe fault to the south (Fig. 1), one of the most active strike-slip faults of Southeast Tibet (Allen et al., 1991). This region is therefore crucial to better understand the horizontal processes generating widening of the plateau, either related to strike-slip faults like the XF (e.g., Tapponnier et al., 2001; Liu-Zeng et al., 2008) or outward flow of lower crust (e.g., Clark et al., 2005a).

* Corresponding author.
E-mail address: anne.replumaz@univ-grenoble-alpes.fr (A. Replumaz).
[1] Present address: Department of Earth Sciences, China University of Petroleum, Beijing 102249, China.

http://dx.doi.org/10.1016/j.epsl.2017.02.025
0012-821X/

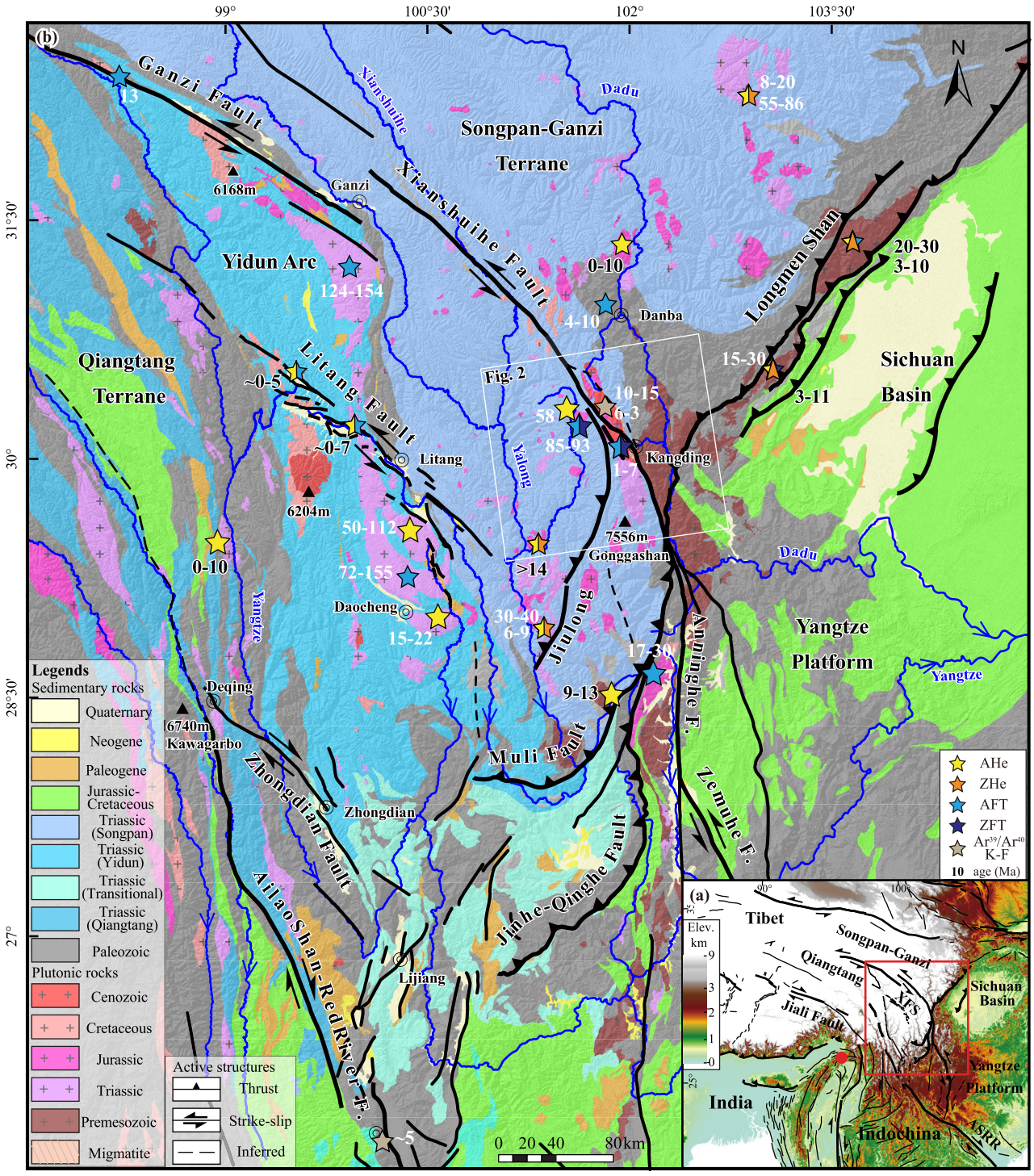

Fig. 1. Tectonic setting of Southeast Tibet. **a)** Topography and active faults of the central and eastern Tibetan Plateau. Red rectangle indicates location of Fig. 1b. Red point: pole of the small circle fitting the Xianshuihe fault system trace. **b)** Geological map of SE Tibet, with thick black lines indicating active faults; blue solid lines are rivers. Stars correspond to thermochronological ages, with different colors according to method (in black period of rapid exhumation deduced from altitudinal profiles, in white individual ages; see text and SM4 for references and locations of published ages). (For interpretation of the references to color in this figure legend, the reader is referred to the web version of this article.)

However, despite the numerous reported Mio-Pliocene fission-track ages in the Gongga batholith, no precise timing and rate of exhumation has yet been inferred, nor precise mechanism to explain such exhumation (e.g.; Xu and Kamp, 2000; Lai et al., 2007; Wilson and Fowler, 2011). In this paper, we present new apatite and zircon fission-track data from the north part of the Gongga batholith. These data span a wider elevation range than previous studies, and allow to perform thermo-kinematic modeling (Braun et al., 2012) in order to precisely constrain the onset and rate of exhumation along three elevation profiles. Each profile recorded a specific exhumation history since the middle Miocene, but they can all be explained by the switch of motion between different fault strands of the XF within a restraining bend. Deciphering this history allows constraining the age of onset of the XF, and thus to discuss its rate and how the building mechanisms of the Tibetan Plateau are expressed locally in Southeast Tibet.

2. Geological setting

The geology of Southeast Tibet is dominated by the Songpan-Ganzi terrane, which corresponds to a thick, intensely folded and deformed Triassic sedimentary sequence that has been detached and thrust upon the Proterozoic basement of South China in the late Triassic and intruded by numerous Triassic and Jurassic granitoids (Fig. 1) (e.g., Burchfiel et al., 1995; de Sigoyer et al., 2014). The only Cenozoic batholith of the region is the Gongga batholith located along the XF (Roger et al., 1995; Li and Zhang, 2013).

2.1. The Xianshuihe fault system

The Xianshuihe fault system comprises four fault segments: Ganzi, Xianshuihe, Anninghe, and Zemuhe–Xiaojiang (Fig. 1; Allen et al., 1991). The Holocene left-lateral slip rate on the Xianshuihe fault (XF) segment has been inferred at 15 ± 5 mm/yr, based on offsets of fluvial terrace deposits and glacial moraines (Allen et al., 1991). The most recent GPS measurements yield left-lateral rates of the Xianshuihe fault system of 10–12 mm/yr (Zhang et al., 2013), 7–15 mm/yr (Liang et al., 2013) and 6–14 mm/yr (Zhao et al., 2015). The fault has been highly active in the last centuries, having produced at least 8 earthquakes of magnitude $\geq$7 since 1725 (Allen et al., 1991).

The remarkable continuity of the XF is interrupted in the Gongga batholith area by three en-echelon fault segments: the Yalahe, Selaha and Zheduotang segments (Allen et al., 1991; Fig. 2). Our observations confirm that the Selaha central segment is active (Fig. 2), with clear cumulative offsets of moraines and valleys. The Holocene left-lateral slip rate on the Selaha segment has been inferred at ~4.6 to 7.2 mm/yr (Allen et al., 1991). This segment has been broken by two earthquakes of magnitude 5.6 and 5.9 in 2014 (Jiang et al., 2015). The southern Zheduotang segment shows no sufficiently clear morphologic offsets to infer a Holocene slip rate (Allen et al., 1991). Nevertheless, this segment is also active and has been partially ruptured by the 2014 earthquakes (Jiang et al., 2015). The northern Yalahe segment, passing by Taizhan, does not show clear morphologic offsets but its trace is outlined by deep valleys and steep fault planes trending NW-SE to N-S that show sub-horizontal striations and fault gouge. We suggest that this segment represents a geological fault, and is most probably not currently active.

2.2. The Gongga batholith

The Gongga batholith extends for 120 km in a NNW-SSE direction along the XF, with a width of ~15 km (Figs. 1, 2). The highest regional peak, the Gongga Shan, culminates at 7756 m, more than 3000 m above the mean plateau elevation (Fig. 3a). The batholith contains biotite granite, granodiorite, and monzogranite, locally porphyric (e.g., CIGMR, 2004; Liu et al., 2006). To the east and north, the batholith intrudes sedimentary rocks of the Songpan-Ganzi domain, mostly of Triassic age (Fig. 2a). The granite intruded during the Miocene, based on whole-rock Rb/Sr ages of 12–10 Ma and a U/Pb zircon age of 12.8 ± 1.4 Ma (Roger et al., 1995). More recent U/Pb analyses on zircon reveal a more complex history of the batholith, with Jurassic ages found together with Miocene ages, between 18 and 12 Ma, and some indications for 5–6 Ma ages, in the northernmost part of the massif (Li and Zhang, 2013; Li et al., 2015; Searle et al., 2016), contrasting with Triassic ages in its southern part (Li et al., 2015; Fig. 2a).

The eastern border of the batholith is a 1–3 km wide migmatite zone following the Yalahe and the eastern part of the Selaha segments of the XF (Fig. 2a). In this zone, vertical foliation and sub-horizontal stretching lineation trending N170 have been described and interpreted to result from intense high-temperature left-lateral deformation along the XF (Roger et al., 1995) or thrusting (Li and Zhang, 2013). U/Pb dating of zircon rims suggests that migmatization occurred during the Oligocene, between 32 and 27 Ma (Li and Zhang, 2013).

The cooling history of the batholith is constrained by few Rb/Sr and Ar/Ar ages as well as zircon (ZFT) and apatite (AFT) fission-track ages (Fig. 2). Whole-rock Rb/Sr, biotite K/Ar, and muscovite, biotite and K-feldspar Ar/Ar ages show two phases of cooling through the ~300 °C isotherm at 15–10 Ma and 5.5–3 Ma (Roger et al., 1995; Wallis et al., 2003; Zhang et al., 2004; Chen et al., 2006; Xu, 2009). West of Kangding city, ZFT and AFT ages within the batholith range from 7.3 to 2.3 Ma and 2.9 to 1.2 Ma, respectively (Xu and Kamp, 2000; Wilson and Fowler, 2011). East of Kangding city, across the XF within the Luding granite, ZFT and AFT ages are significantly older: 25.1–16.8 and 14.3–4.5 Ma, respectively (Xu and Kamp, 2000; Wilson and Fowler, 2011). Apatite (U–Th)/He (AHe) ages are between 1.8 and 3.5 Ma, suggesting rapid recent cooling (Clark, 2003).

2.3. Timing of exhumation at the eastern margin of the Tibet Plateau

Low-temperature thermochronology studies have shown that wide portions of SE Tibet, characterized by low relief and high elevation, have experienced little denudation since the Cretaceous (Fig. 1): AHe ages range from 50 to 112 Ma (Clark et al., 2005b) and AFT ages from 72 to 155 Ma (Reid et al., 2005; Lai et al., 2007) in a pluton north of Daocheng; AFT ages range from 124 to 154 Ma in a similar pluton south of Ganzi (Lai et al., 2007); AFT ages in Triassic sandstone east of the Litang fault are older than 70 Ma (Wilson and Fowler, 2011).

Younger ages reflect local exhumation linked to Cenozoic structures (Fig. 1). AFT ages $<$13 Ma along the northernmost segment of the Xianshuihe fault system, the Ganzi fault, have been inferred to indicate activity of the fault since that time (Wang et al., 2009). Southwest of the XF, the Jiulong thrust fault was activated between 9 and 6 Ma, as inferred from AHe ages, but also between 40 and 30 Ma, according to ZHe ages (Zhang et al., 2016). The Muli thrust was activated between 13 and 9 Ma, as inferred from AFT and AHe ages (Clark et al., 2005b). The left-lateral/normal Litang fault system was activated between 5 and 7 Ma, according to AFT and AHe ages (Zhang et al., 2015). Apatite and zircon FT and (U–Th)/He data suggest that the Longmen Shan thrust belt east of the XF experienced two major Cenozoic phases of cooling and exhumation, the first starting at 30–20 Ma (Wang et al., 2012; Tan et al., 2014), and the second starting at 11–8 Ma, with a possible significant decrease in exhumation rate since 2–3 Ma (Arne et al., 1997; Kirby et al., 2002; Godard et al., 2009). Miocene AFT and AHe ages have also been obtained along deeply incised valleys (Fig. 1) and suggest incision initiating $<$10 Ma along the Dadu River (Clark et al., 2005a; Ouimet et al., 2010), $<$14 Ma along the Yalong River (Ouimet et al., 2010), $<$10 Ma along the Yangtze River (Ouimet et al., 2010), and $<$22 Ma along a Yangtze tributary south of the Daocheng pluton (Tian et al., 2014).

3. Methods

3.1. Sampling strategy

In order to explore the thermal history of the Gongga batholith and its link to the XF, we collected 21 samples for fission-track analysis, aiming to combine horizontal profiles across the fault zone and altitudinal transects (Fig. 2). We collected 10 samples across the range and the XF at the level of Kangding city (Fig. 4), 8 west of the fault (upper Kangding transect) and 2 east of the fault (Luding transect). The Longbu transect, crossing the range west of Longbu village, yielded 5 samples. The Taizhan transect,

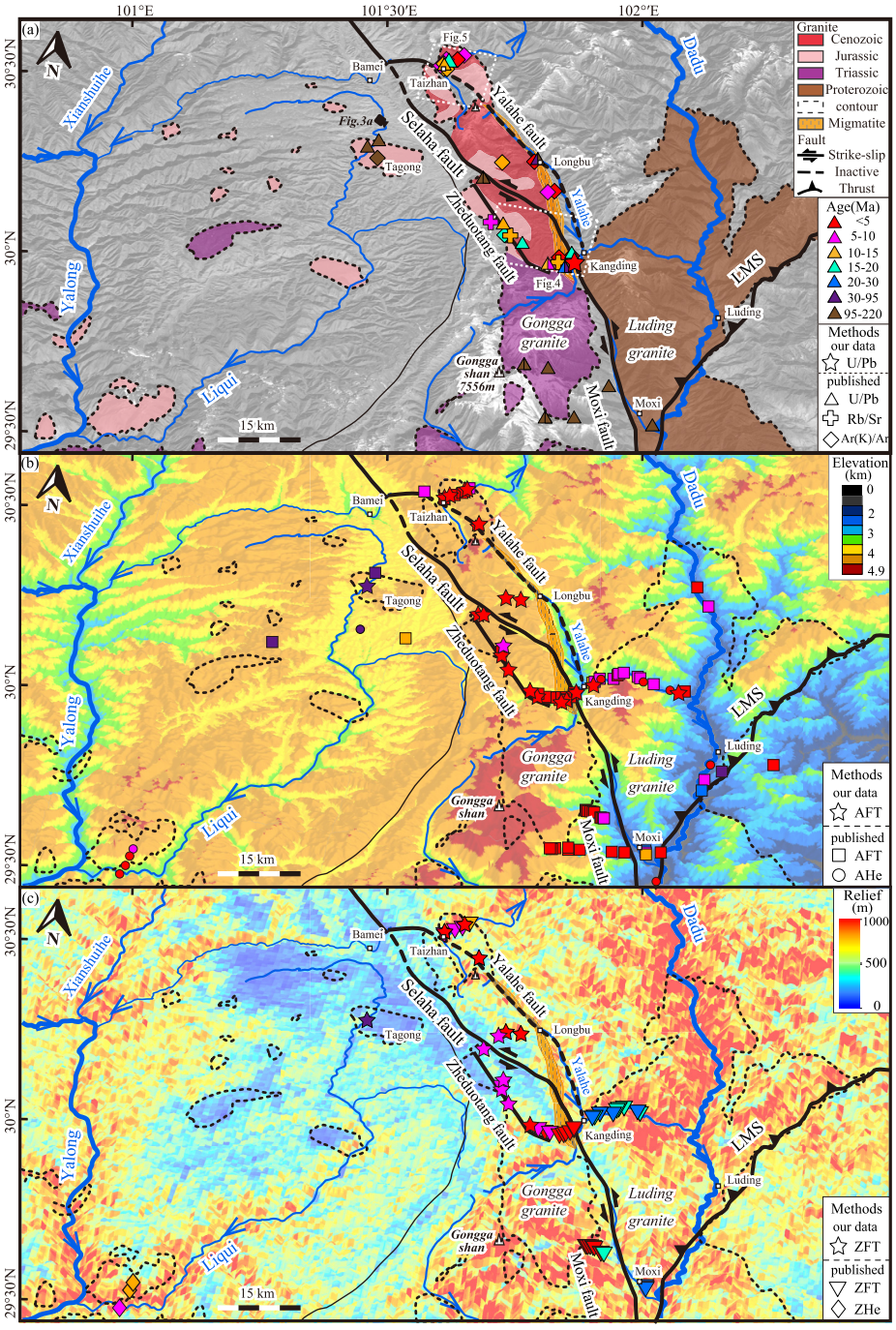

Fig. 2. Morphology, geology and thermochronology of the Gongga batholith. **a)** Map of faults (thick black lines, dotted when inactive or inferred), granites (colored according to age) and rivers (blue). Individual U/Pb (star: this study; triangle: published), Rb/Sr (cross), and Ar/Ar (diamond) ages colored according to age. **b)** DEM with AFT (star: this study; square: published) and AHe (circle) ages colored according to age. **c)** Relief map with ZFT (star: this study; inverse triangle: published) and ZHe (diamond) ages colored according to age. See supplementary material for references and locations of published ages. (For interpretation of the references to color in this figure legend, the reader is referred to the web version of this article.)

crossing the northernmost part of the Gongga batholith east of Taizhan village, yielded 4 samples (Fig. 5). One sample was also collected from the Triassic Tagong monzogranite on the Bamei Plateau (Fig. 2). We obtained 33 ZFT and AFT ages (Tables 1, 2). The ZFT and AFT thermochronometers are sensitive to temperature ranges of 200–240 °C and 80–120 °C, respectively, depending on cooling rate (Brandon et al., 1998; Reiners and Brandon, 2006; Bernet, 2009). Therefore, their combination can be used to constrain exhumation and denudation in the upper crust from depths between ∼3.5 and ∼7 km, depending on the local geothermal gradient.

As both our AFT and ZFT ages and those from the literature are especially young in the migmatites of the Kangding profile, we sampled a dyke in that area (CD10-1, Fig. 3c, d) for U/Pb dating, in order to verify whether a late magmatic event, undetected in previous studies, could have affected that area. Sample CD10-1 was analyzed with LA-ICP-MS at the Laboratoire Magma et Volcans in Clermont-Ferrand, France (see SM1 for details).

3.2. Apatite and zircon fission-track analytical methods

Samples were prepared and analyzed at ISTerre (Grenoble, France), using the external detector method. Samples were irra-

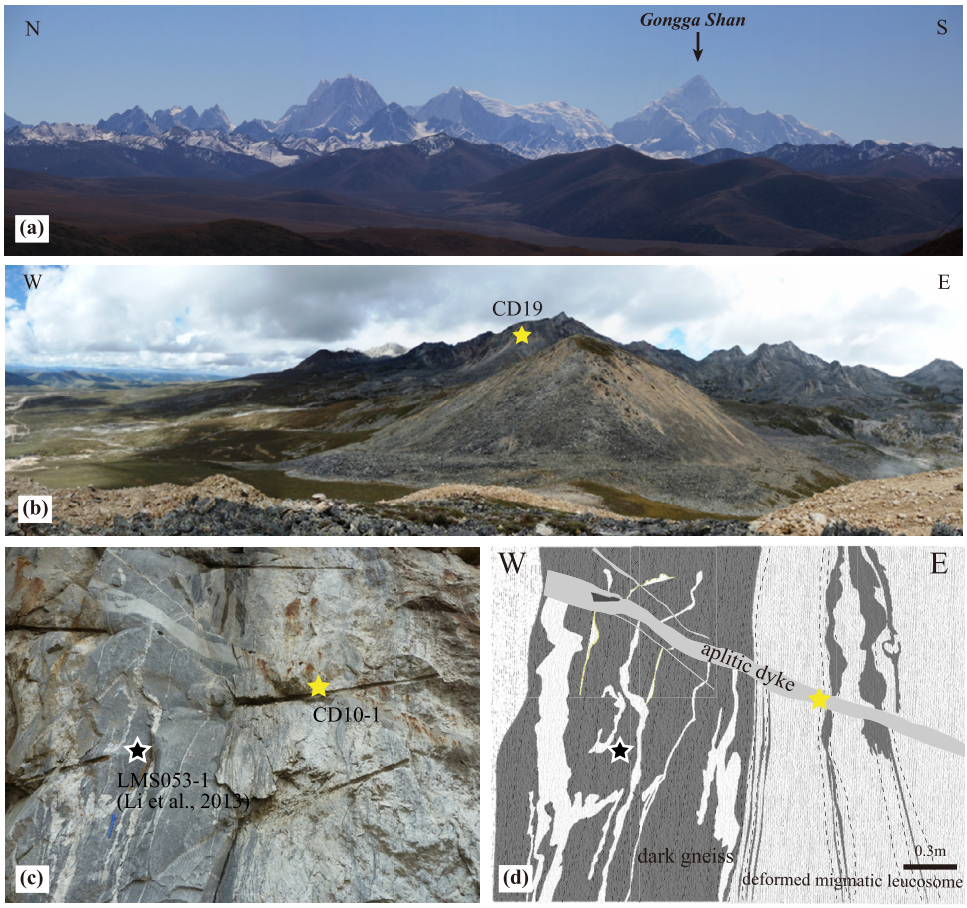

Fig. 3. Field photographs. **a)** View of the Gongga Shan standing more than 3000 m above the mean plateau elevation (see view location on Fig. 2b). **b)** View of the highest altitude samples of the Kangding transect (see view location on Fig. 4). **c)** Outcrop in the migmatite zone, with location of sample CD10-1, used to date Pliocene dyke injection at ~4 Ma (U/Pb). **d)** Corresponding sketch.

diated in the FRM II Research Reactor at the Technische Universität München (Germany) together with IRMM540R and IRMM541 dosimeter glasses for apatite and zircon, respectively. At least 20 grains per sample were analyzed and fission-track ages were calculated using the BINOMFIT program by M. Brandon (cf. Ehlers et al., 2005). The weighted-mean apatite and zircon Zeta values for Yuan-Ze Zhang are respectively 311 ± 8.5 and 145 ± 2.8, based on Durango, Fish Canyon Tuff, and Buluk Tuff age standards.

3.3. Data interpretation and thermo-kinematic modeling

Owing to the low uranium content and young cooling ages of apatite grains, we did not obtain sufficient horizontally confined track-length as well as etch-pit-width (Dpar) measurements to be statistically representative. We therefore do not use thermal-history modeling using these kinetic indicators but rather exploit our multi-method thermochronology and the spatial relationships between our samples for thermal-kinematic modeling. Initial semi-quantitative interpretation of the data uses age-elevation relationships between the samples. We calculate the Bayesian information criterion (BIC) to test if the age-elevation profiles could be better fit by a single slope or multiple independent slope segments, the preferred model being the one yielding the lowest BIC value (Glotzbach et al., 2011).

We employed the three-dimensional thermal-kinematic code Pecube to quantify the exhumation history combining the results from each thermochronometer (Braun, 2003; Braun et al., 2012). The Kangding, Longbu and Taizhan transects have been separated as independent profiles (see Pecube model zones on Figs. 4, 5). For all zones, the upper model boundary corresponds to the present-day surface topography, derived from the Shuttle Radar Topography Mission (SRTM) digital elevation model reduced to a resolution of 500 m. The lower model boundary is fixed at 50 km depth, which corresponds to the crustal thickness in this area (e.g., Wang et al., 2010). Surface temperatures were calculated using an atmospheric lapse rate of 4 °C/km and a temperature at sea level of 25 °C (Bermúdez et al., 2011; Zhang et al., 2015). Other physical parameters are fixed to standard values (see SM2). The geothermal gradient and related basal temperature are crucial parameters that need to be constrained to obtain robust results (Bermúdez et al., 2011; Glotzbach et al., 2011). A high resampling ratio of 90% was set, implying a slow convergence rate for the inversion, but ensuring sufficient exploration of the parameter space.

4. Results: crystallization and cooling of the Gongga batholith

4.1. U/Pb ages

CD10-1 is a thin aplitic dyke that was sampled at site CD10 (Fig. 3c, d). The dike appears undeformed and cuts across migmatitic gneiss and thin folded leucocratic levels. Twenty-nine spot analyses on sample CD10-1 yield a lower intercept age of 4.00 ± 0.06 Ma (Fig. 6d), which is equivalent within error limits to the weighted-average $^{206}Pb/^{238}U$ age (see SM1 for further precision). At the same outcrop, zircons from the melanosome have yielded U/Pb ages of 26.9 ± 0.9 Ma for the rims (Li and Zhang, 2013).

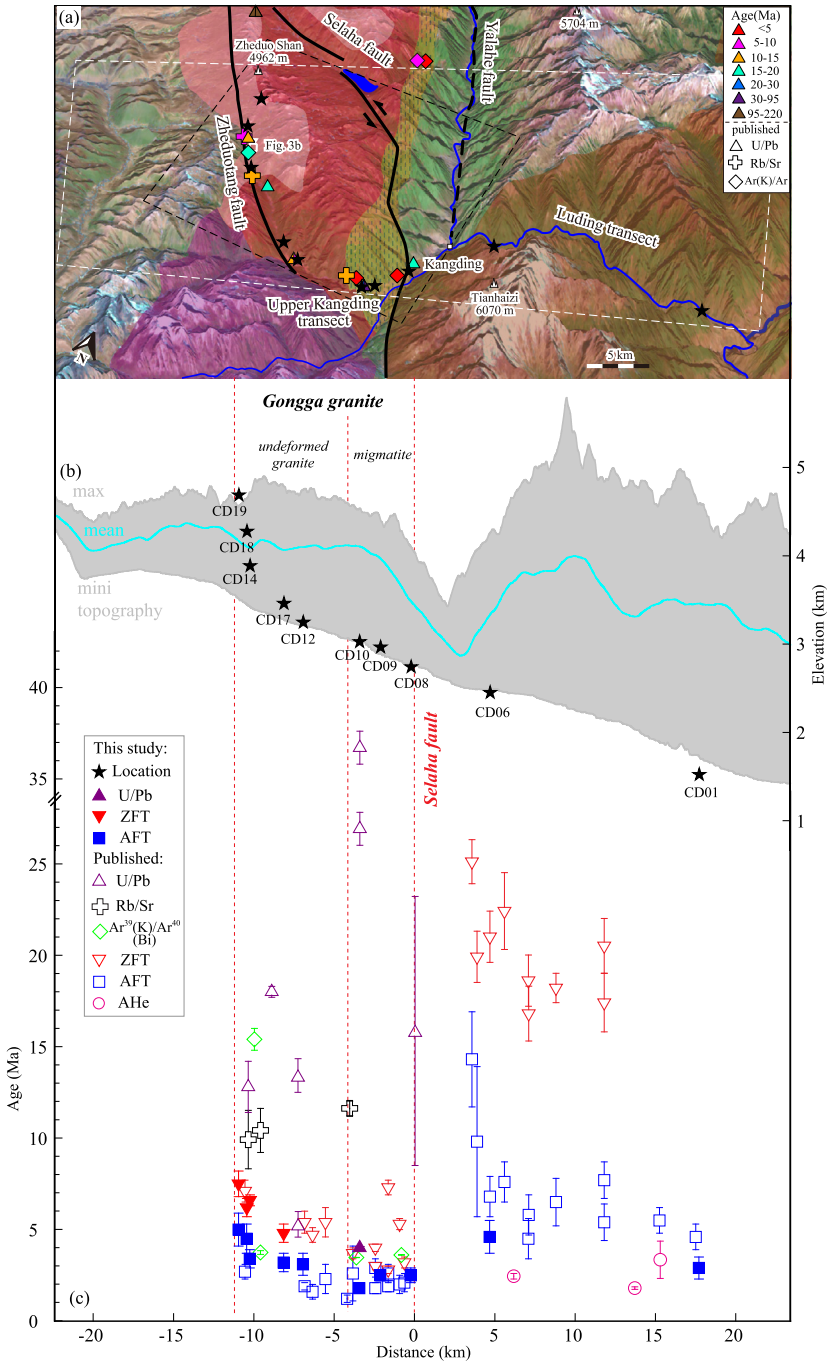

Fig. 4. a) Geological map of the Kangding area (see location on Fig. 2a), with our sample locations (black stars) and published geochronologic and thermochronologic ages (colored according to age, shapes indicate different methods); dashed line outlines Pecube model zone. **b)** Envelope of topography along the transect, located within dashed line contour on a), with vertical position of the samples. **c)** ENE-WSW projection of the geo/thermochronologic ages versus distance from Xianshuihe fault (XF) along the Kangding/Luding transect (our ages shown with filled symbols, published ages with empty symbols). See SM4 for references and locations of published ages. (For interpretation of the colors in this figure, the reader is referred to the web version of this article.)

4.2. Fission-track data

From the 21 samples collected along 3 transects across the Gongga batholith, we obtained 20 AFT ages (Table 1) and 11 ZFT ages (Table 2). AFT ages are all Pliocene (1.8 ± 0.2 to 5.0 ± 0.9 Ma), and ZFT ages are late Miocene to Pliocene (2.8 ± 0.2 to 7.5 ± 0.7 Ma), except for sample G16 from the Tagong Monzogranite, which yielded Cretaceous AFT (88 ± 4 Ma) and ZFT (93 ± 6 Ma) ages. Chi-square probabilities of all samples are >5% and age dispersions close to 0, indicating that the samples contain a single age population and are not affected by significant partial annealing. Sample locations were projected onto two ENE-WSW swaths across the central and northern Gongga massif (Kangding–Luding and Taizhan transects), to analyze trends of FT ages versus distance from the XF (Figs. 4, 5). The Longbu transect is cut by the most active segment of the XF (Selaha segment, Fig. 2), and is presented in SM3.

4.2.1. Kangding transect

The 30 km long Kangding transect stretches from 1520 m elevation along the deeply incised Kangding valley, up to 4680 m at the western border of the Gongga batholith. Two zones have been

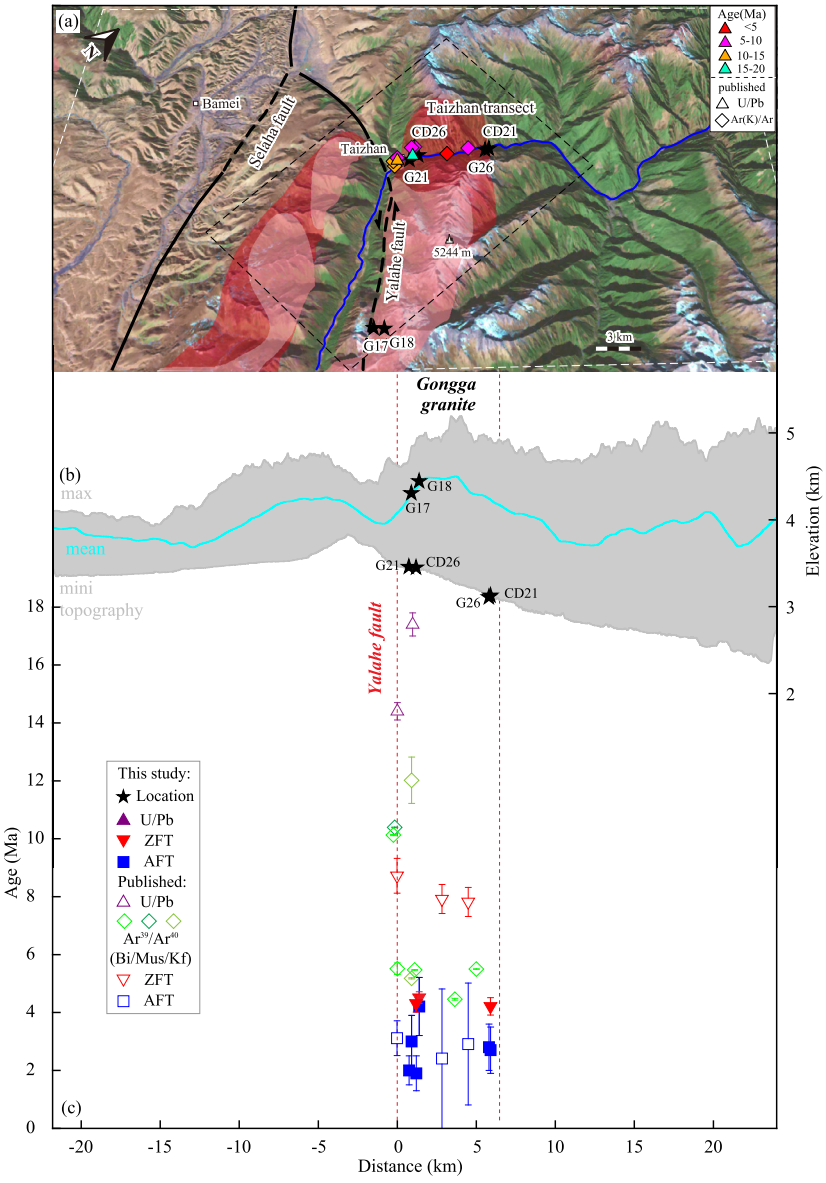

Fig. 5. Geological map, topographic cross-section and thermochronology data of the Taizhan area (see location on Fig. 2b); same legend as Fig. 4.

distinguished: the migmatite zone along the Selaha segment and the undeformed granite, at higher elevation farther from the fault (Fig. 4).

We collected five samples from the granites forming the highest part of the range, along the upper part of the transect spanning ~3200 m to ~4700 m elevation and ~13 km distance (CD12, 14, 17–19). The 5 samples yield AFT ages between 3.1 ± 0.6 and 5.0 ± 0.9 Ma (Table 1) that show a positive age-elevation relationship (AER) that can be fit by a single least-squares regression slope of 0.77+0.7 −0.25 km/Myr with a high correlation coefficient ($r^2 = 0.93$; Fig. 6a). This single AER fit has a lower BIC value (5.95) than that of a two-tier fit (9.09), suggesting that it is the best-fit solution and that our data reflect a single exhumation episode. The 0-age intercept depth of the AER is 2.1 km below the surface, which is fairly shallow for commonly assumed values of the geothermal gradient (~30 °C/km; see below for an assessment of this value) and would imply slowing of exhumation since the AFT cooling age of the lowest sample (CD12, 3.1 ± 0.6 Ma, 3242 m). A few horizontally confined track lengths have been measured only for samples CD17 and CD19; all are >13 µm.

The four ZFT ages (CD14, 17-19) range between 4.8 ± 0.5 and 7.5 ± 0.7 Ma (Table 2), 2 to 3 Ma older than the AFT ages for the same samples (Fig. 6a). The positive AER can be fit by a single least-squares regression slope of 0.58+0.32 −0.16 km/Myr with a BIC of 6.17 and a correlation coefficient of 0.76. A two-phase AER, with exhumation rates of ~1.7 km/Myr from 7.5 to 6 Ma dropping to 0.24+0.11 −0.06 km/Myr between 6 and 4.5 Ma, has nearly the same BIC (6.89) and is also compatible with our data.

We collected three samples from the migmatites at elevations ranging from ~2700 to ~3000 m and over <5 km distance (CD8–10). AFT ages of these samples are between 1.8 ± 0.6 and 2.5 ± 0.4 Ma, with no clear AER (Table 1; Fig. 4).

4.2.2. Luding transect

Two samples (CD1 and 6) from the Proterozoic Luding basement granitoids east of the XF (Fig. 4) have AFT ages of 2.9 ± 0.6 and 4.6 ± 0.9 Ma. Taken at face value, these two samples with an elevation difference of 930 m would suggest Pliocene exhumation at a rate of 0.55 km/Myr from 5 to 3 Ma (Fig. 6b). Our AFT ages appear slightly younger than previous estimates (Xu and Kamp, 2000;

Table 1
Apatite fission track data.

Transect	Sample	Long. E°	Lat. N°	Ele. (m)	Grain (N)	ρ_d (10^5 cm^{-2}) (Nd)	ρ_s (10^4 cm^{-2}) (Ns)	ρ_i (10^5 cm^{-2}) (Ni)	U (ppm)	P(χ^2) (%)	Central age $\pm1\sigma$ (Ma)	Dpar $\pm1\sigma$ (μm)	MTL $\pm1\sigma$ (μm) (Nl)
Kangding	CD01-1	102.1360	30.0732	1520	22	8.684 (5548)	2.72 (21)	11.7 (902)	20	97.2	2.9 ± 0.6	1.67	
	CD06-1	101.9932	30.0597	2451	26	8.656 (5530)	2.96 (24)	7.94 (643)	14	98.7	4.6 ± 0.9	1.63	
	CD08-1	101.9540	30.0200	2738	23	8.628 (5513)	4.26 (32)	20.7 (1555)	36	99.7	2.5 ± 0.4	1.48	
	CD09-2	101.9423	29.9958	2961	24	8.600 (5495) 8.572	4.62 (47)	22.8 (2316)	40	94.0	2.5 ± 0.3	1.41	14.11 ± 0.49 (2)
	CD10-3	101.9365	29.9899	3022	26	8.572 (5477)	4.67 (45)	32.5 (3133)	57	95.1	1.8 ± 0.2	1.51	13.57 ± 0.46 (3)
	CD12	101.8881	29.9941	3242	26	8.544 (5459)	1.88 (26)	7.51 (1039)	13	96.0	3.1 ± 0.6	1.49	
	CD17	101.8737	30.0022	3456	37	8.384 (5357)	2.06 (37)	7.76 (1391)	14	90.9	3.2 ± 0.5	2.08	13.95 ± 0.58 (2)
	CD14-4	101.8254	30.0450	3880	38	8.360 (5343)	1.59 (34)	5.60 (1196)	10	92.1	3.4 ± 0.5	1.87	
	CD18	101.8075	30.0761	4270	37	8.408 (5372)	1.52 (30)	4.10 (812)	7	99.4	4.5 ± 0.8	1.73	
	CD19	101.8077	30.0942	4680	30	8.431 (5387)	3.08 (29)	7.45 (701)	13	99.4	5.0 ± 0.9	2.03	14.28 ± 0.32 (5)
Longbu	G10	101.7449	30.1849	4387	27	10.47 (4536)	2.41 (32)	10.2 (1354)	12	97.8	3.6 ± 0.6	1.57	
	G11	101.7548	30.1853	4302	20	10.54 (4545)	1.87 (19)	8.78 (920)	10	98.0	3.4 ± 0.7	1.33	
	G14	101.7842	30.2560	3738	23	10.68 (4565)	2.16 (24)	12.9 (1434)	15	95.7	2.7 ± 0.5	1.51	
	G15	101.8127	30.2614	3514	24	10.74 (4574)	1.93 (28)	12.1 (1775)	14	99.9	2.6 ± 0.4	1.69	
Taizhan	G17	101.6954	30.4492	4297	24	10.88 (4594)	0.694 (9)	3.81 (494)	4	98.9	3.0 ± 0.9	1.50	
	G18	101.7006	30.4515	4434	21	10.95 (4603)	1.88 (19)	7.47 (756)	8	94.6	4.2 ± 1.0	1.64	
	G26	101.6537	30.5795	3102	26	11.09 (4622)	0.638 (9)	3.84 (541)	4	85.7	2.8 ± 0.8	1.49	
	CD21-1	101.6520	30.5821	3120	30	8.516 (5441)	0.735 (9)	3.38 (414)	6	89.9	2.7 ± 0.8	1.61	
	G21	101.6237	30.5420	3432	28	11.02 (4613)	0.927 (13)	7.82 (1096)	9	92.1	2.0 ± 0.5	1.47	
	CD26-4	101.6242	30.5459	3442	26	8.488 (5423)	0.613 (7)	4.09 (467)	7	82.1	1.9 ± 0.6	1.56	
Tagong	G16	101.5219	30.2612	3572	22	10.81 (4584)	104 (1316)	19.2 (2429)	22	85.9	87.5 ± 3.9	1.43	

Note: Brackets show number of tracks counted and measured. Standard and induced tracks were measured on mica external detector ($g = 0.5$) and fossil track densities on internal grain surfaces. All ages in the table are pooled ages, with errors reported at the one sigma level. Abbreviations: $\mu_{s/i/d}$, spontaneous/induced/standard glass track densities; Ns/i/d, numbers of spontaneous/induced/standard glass tracks; N, number of grains; MTL, mean confined horizontal track length; Nl, number of lengths.

Wilson and Fowler, 2011). The positive AER of all the available AFT data from this transect can be fit by a single least-squares regression slope of 0.33+0.11 −0.06 km/Myr from 5 to 3 Ma (Fig. 6b). The BIC value is high (32.78), probably due to the dispersion of the data. A two-phase AER with a similar BIC value is also compatible with the data, suggesting nearly no exhumation (∼0.01 km/Myr) until ∼6 Ma followed by exhumation at 0.29+0.09 −0.05 km/Myr until ∼3 Ma (Fig. 6b). Published ZFT ages range between 17 and 25 Ma, much older than AFT ages (∼14 Ma), indicating relatively slow exhumation east of the XF during the Miocene, at a rate of ∼0.1–0.22 km/Myr (Xu and Kamp, 2000). Three published AHe ages (Clark et al., 2005b) show no clear slope but a general trend that is steeper than the slope of the AFT AER, possibly suggesting faster exhumation after ∼3 Ma.

4.2.3. Taizhan transect

The Taizhan transect is located east of the XF at elevations varying from 3400 m to 3100 m within 10 km, along a tributary valley of the Dadu River, incised more than 2000 m below the mean plateau elevation (Fig. 5). Four samples (G21, G26, CD21, CD26) from a biotite monzogranite yield AFT ages between 1.9 ± 0.6 and 2.8 ± 0.8 Ma (Table 1), with a poor correlation with elevation (Fig. 6c). The measured AFT ages are similar to published data (Xu and Kamp, 2000). ZFT ages range between 4.0 ± 0.3 and 4.2 ± 0.3 Ma (Table 2), with a positive correlation with elevation (Fig. 6c). They are significantly younger than previously reported ages between 8 and 9 Ma (Xu and Kamp, 2000). Two samples located ∼13 km to the southeast and at higher elevations of 4300–4400 m (G17–18) show similar AFT and ZFT ages. When plotted together with the ages from the Taizhan transect, these data show an AER with a slope of 1.08+3.0 −0.46 km/Myr between 2 and 3 Ma, whereas the slope for ZFT ages is 2.82+6.42 −1.16 km/Myr (r^2 = 0.99, BIC =0.95) at ∼4 Ma. The difference in AFT and ZFT age for the same sample is less than 2 Ma, suggesting rapid cooling between ∼4 and ∼2 Ma.

Table 2
Zircon fission track data.

Transect	Sample	Grains (N)	ρ_d (10^5 cm^{-2}) (Nd)	ρ_s (10^4 cm^{-2}) (Ns)	ρ_i (10^5 cm^{-2}) (Ni)	U (ppm)	P(χ^2) (%)	Central age $\pm 1\sigma$ (Ma)
Kangding	CD17	20	2.769 (4421)	1.72 (570)	7.11 (2358)	1022	86.2	4.8 ± 0.5
	CD14-4	21	2.773 (4427)	4.85 (623)	12.8 (1647)	1840	65.8	6.6 ± 0.3
	CD18	20	2.765 (4415)	2.18 (406)	6.88 (1279)	990	99.6	6.2 ± 0.5
	CD19	24	2.761 (4410)	3.51 (769)	9.34 (2047)	1346	91.0	7.5 ± 0.7
Longbu	G11	15	3.472 (4203)	4.47 (862)	11.8 (2276)	1352	76.0	7.6 ± 0.4
	G13	20	3.453 (4199)	2.11 (795)	7.96 (3002)	918	85.0	5.3 ± 0.2
	G14	19	3.435 (4196)	1.45 (542)	8.82 (3291)	1023	83.0	3.3 ± 0.2
	G15	15	3.417 (4192)	0.609 (199)	4.22 (1379)	491	90.0	2.8 ± 0.2
Taizhan	G18	15	3.380 (4185)	2.88 (496)	12.5 (2148)	1471	89.6	4.5 ± 0.2
	G26	17	3.344 (4177)	1.08 (247)	5.30 (1208)	631	99.8	4.0 ± 0.3
	G21	15	3.362 (4181)	1.53 (282)	7.07 (1301)	837	95.9	4.2 ± 0.3
Tagong	G16	16	3.399 (4188)	14.4 (1673)	3.03 (351)	354	96.0	92.8 ± 5.7

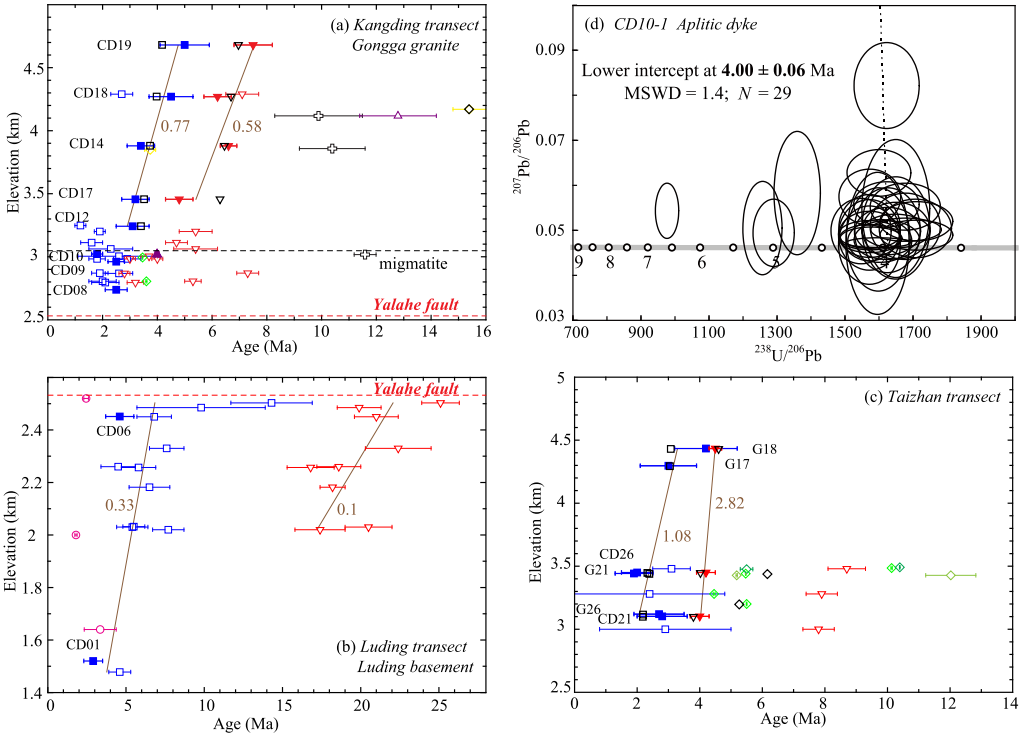

Fig. 6. (a–c) Age–elevation relationships (AER). Least-square fits are calculated assuming one (brown) or two (gray) exhumation stages, for AFT (blue squares) and ZFT (red triangles) ages. Bayesian Information Criterion (BIC) and best-fit slopes are marked with the same color. Black open symbols indicate ages predicted by Pecube inversion. Published geochronologic and thermochronologic ages are shown for reference (open symbols, colored according to method; see Fig. 4 for legend and supplementary material for references). **a)** Upper Kangding transect. **b)** Luding transect. **c)** Taizhan transect. **d)** U/Pb Tera–Wasserburg plot for zircons of sample CD10-1 from an undeformed dyke along the Upper Kangding transect (purple triangle on a). (For interpretation of the references to color in this figure legend, the reader is referred to the web version of this article.)

5. Three-dimensional thermal-kinematic modeling

In order to combine the results from the different thermochronometers and to better constrain the recent exhumation history, we conducted three-dimensional thermal-kinematic modeling using the *Pecube* code (Braun, 2003; Braun et al., 2012) for two zones of the Gongga batholith; the upper part of the Kangding transect and the Taizhan transect, where our data are most abun-

dant. Parameter values for the modeling are reported and justified in SM2.

5.1. Upper Kangding transect

For this model, we use five samples that have both AFT and ZFT ages from within the granite located at the highest elevations, above the migmatite zone (CD12, 14, 17, 18, 19; Fig. 4). All samples are located east of the Zheduotang fault, which is not taken into account in the modeling. To constrain high-temperature cooling, we use a published biotite K/Ar age of 15.4 ± 0.6 Ma located along the same transect (Xu, 2009), interpreted as a maximum age of cooling through the 300 ± 25 °C isotherm.

The model runs for 19 Myr and assumes a three-stage cooling history with two transition times: T_1 prior to ZFT ages between 19 and 6 Ma, and T_2 between 6 and 0 Ma. Exhumation rates during the second phase (E1) and the third phase (E2) can vary from 0 to 4 km/Myr. The relief factor R = h1/h2, defined as the ratio between the initial (h1) and present-day relief (h2) (Valla et al., 2010), can vary between 0 and 1, and the basal temperature between 600 and 1400 °C, corresponding to a near-surface geothermal gradient between ~25 and ~45 °C/km.

The inversion results show that a three-stage history is well constrained, and fits the data well. All predicted ages are within the 1σ-error bar of the observed ages, except for the lowest ZFT age (Fig. 6a). The best-fit solutions have an onset time T_1 of the second exhumation phase ranging from 8 to 10 Ma, with a maximum probability at 8.6 ± 0.5 Ma (Fig. 7a). The exhumation rate E_1 is between 1.5 and 2.5 km/Myr, with a maximum probability at 1.85 ± 0.2 km/Myr (Fig. 7b). This rate is consistent with rapid exhumation at ~1.74 km/Myr, deduced from the 3 highest ZFT samples (Fig. 6a). After T2, around 3–5 Ma with a maximum probability at 4.0 ± 0.4 Ma, the exhumation rate E_2 decreases, with a maximum probability at a rate of 0.75 ± 0.1 km/Myr, consistent with the rate of 0.77 km/Myr deduced from the AER for AFT ages between 3 and 5 Ma (Fig. 6a). The best-fit basal temperature is high, at 1375 °C, close to the maximum allowed, corresponding to a near-surface thermal gradient of 41.5 °C/km. R is close to zero, indicating significant relief growth during the model run.

5.2. Taizhan transect

A Pecube model for a three-stage cooling history was also attempted to fit the data obtained along the Taizhan transect, east of the Yalahe segment of the XF (Fig. 2). The common parameters were set as for the upper Kangding transect. This model is constrained by AFT and ZFT ages from 6 samples (G17–18, G21, G26, CD21, CD26). To constrain high-temperature cooling, we use Ar/Ar mica ages that range from ~4.5 to 5.5 Ma (Zhang et al., 2004; Wallis et al., 2003), obtained on samples close to ours (Fig. 5). Two samples, located along the Yalahe fault, have older Ar/Ar mica ages between 10 and 12 Ma and are not included in our modeling. The significance of these older ages is discussed in the following section. The model fits our FT data well, with all the predicted ages within the 1σ-error bar for the AFT and ZFT results. Predicted Ar/Ar ages are also close to the younger observed Ar/Ar ages (Fig. 6c). The best-fit solutions have an onset time of rapid cooling T_1 ranging from 5 to 7 Ma, with a maximum probability at 5.6 ± 0.4 Ma (Fig. 7a). The exhumation rate E_1 is high, between 3–4 km/Myr, with a maximum probability at ~4 km/Myr, slightly higher than the estimation from the ZFT AER (~2.82 km/Myr). The exhumation rate decreases after ~2–3 Ma, with a most probable rate of 0.94 km/Myr, close to that estimated from the AFT AER (~1.08 km/Myr).

6. Discussion: cooling history of the Gongga batholith and implications for the kinematic evolution of SE Tibet

6.1. Oligo-Miocene migmatization

The migmatites show steep foliations trending ~N170 and sub-horizontal stretching lineations which were interpreted as reflecting left-lateral shear coeval to partial melting along the XF (Roger et al., 1995). Assuming that the age of melting corresponds to that of the nearby undeformed granite would imply that the left-lateral XF was active prior to ~13 Ma (Roger et al., 1995). However Li and Zhang (2013) provided new U/Pb ages showing that the Migmatites are in fact Oligocene (32–27 Ma), and further suggest that migmatization was linked to an early phase of thrusting along the XF. The granite emplacement, now estimated to last from ~18 to ~12 Ma (Li and Zhang, 2013; Searle et al., 2016), took place after the migmatization and associated deformation. Therefore the age of the granite does not constrain the onset of the left-lateral XF and rather post-dates both the Oligocene migmatization and the Miocene intrusions.

6.2. Mio-Pliocene thermal and exhumation history of the Gongga batholith

The Miocene event is related to a large amount of melting; the associated thermal perturbation has reset the FT thermochronometers with all FT ages being younger than 9 Ma. Our U/Pb zircon age at ~4 Ma on an undeformed aplitic dyke that cuts across the migmatitic gneiss is much younger than the previous U/Pb ages (Fig. 3c, d) and documents a fifth magmatic episode. A similar U/Pb age at ~5 Ma has recently been documented along the same transect, showing a very complex age pattern interpreted as representing partial melting (Searle et al., 2016). These new U/Pb ages reveal a limited early Pliocene (4–5 Ma) pulse of partial melting that did not affect the entire batholith (Fig. 4). The spatial distribution of young high-temperature (Rb/Sr, K/Ar, Ar/Ar) ages highlights the zones where the thermal imprint of the early Pliocene partial melting event has been strong. In the eastern part of the Taizhan section, Ar/Ar ages range from 4.5 to 5.5 Ma; in the lower Kangding section Ar/Ar ages are ~3.5 Ma (Wallis et al., 2003; Zhang et al., 2004; Fig. 4b, SM4). In contrast, in the western part of the Taizhan section, along the Yahale fault, Ar/Ar cooling ages recording the 18–12 Ma (middle Miocene) magmatic event have been preserved (Fig. 5b), whereas in the upper part of the Kangding section, both Ar/Ar and FT ages older than 5 Ma are preserved (Fig. 4b). Thus, early Pliocene partial melting and associated heating was localized and did not affect thermochronological systems throughout the batholith. Away from the zones where this late-stage dyke intrusion occurred, the thermochronology data can be used to infer the exhumation history of the batholith.

Along the upper part of the Kangding transect, our AFT and ZFT ages between 3 and 8 Ma can be modeled as resulting from a phase of rapid exhumation since 8.6 ± 0.5 Ma, with a most probable rate of ~1.85 km/Myr, considering a most probable thermal gradient of 41.5 °C/km. These timing and rate correspond to ~9 km of exhumation or ~375 °C of cooling. The onset of exhumation took place ~3 Myr after the end of the Miocene magmatic pulse that occurred between 18 and 12 Ma (Li and Zhang, 2013). Simon-Labric (2011) studied the effect of magma intrusions on low-temperature thermochronology data and showed that if the intrusion is long-lived, as in a magmatic arc, the geothermal gradient can be perturbed and raised to high stable values, for a long time period and in a region larger than the intrusion itself. The AER slope shows a perturbation during the period corresponding to the intrusion, but after reaching a new steady-state with high geothermal gradient, the slope of the AER again indicates

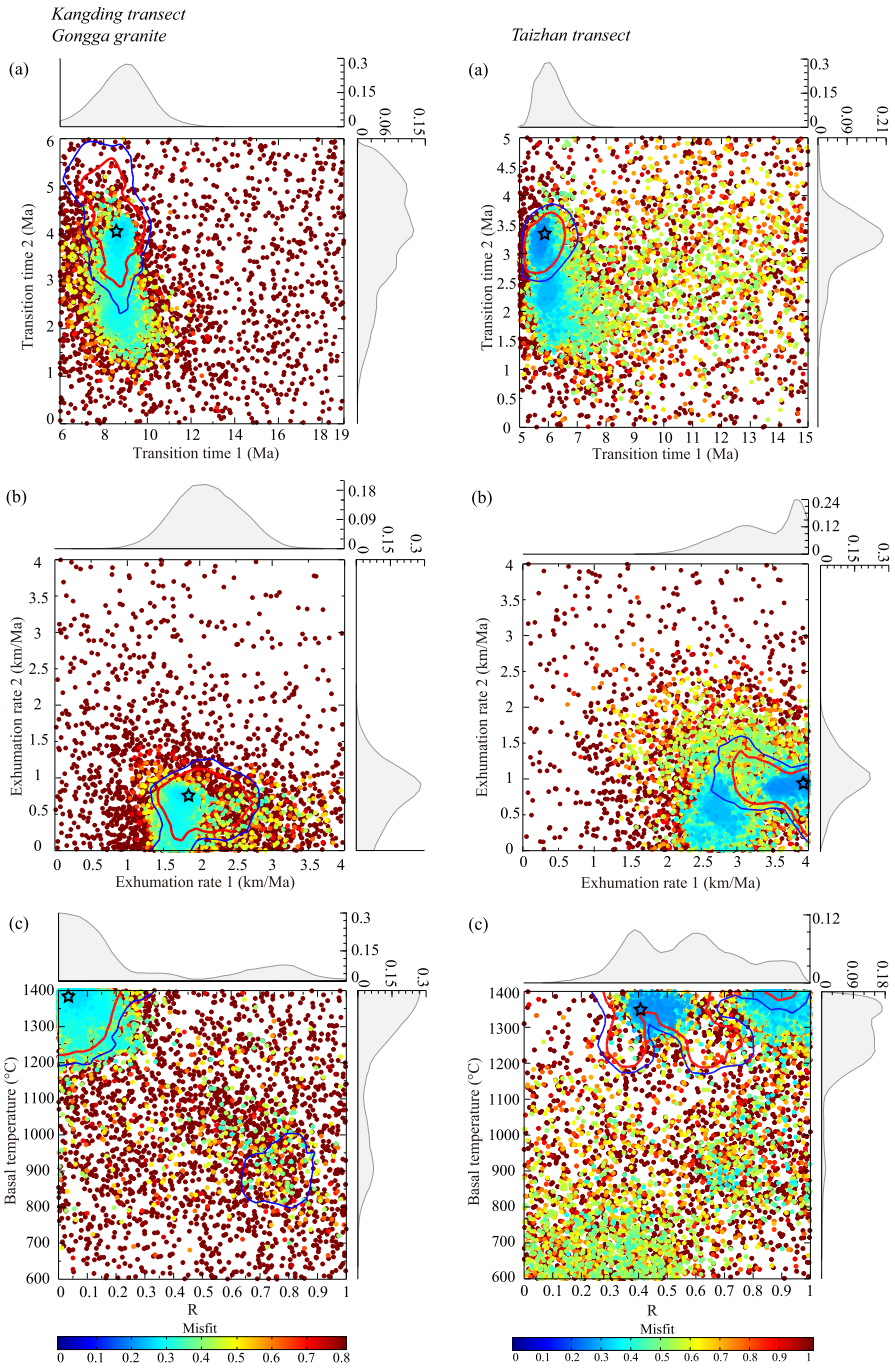

Fig. 7. Pecube inversion results for ZFT and AFT data from the Upper Kanding and Taizhan transects, shown as 2D scatter plots of inversion results and 1D posterior probability-density functions (PDFs) of parameter values. Points correspond to individual forward models, colored by misfit value (common scale). The optimal solution is shown by a star with 2σ (blue) and 1σ (red) confidence contours. **a)** Transition times: T1: onset of first exhumation phase; T2: onset of second exhumation phase. **b)** Exhumation rates of the first (E1) and the second (E2) exhumation phases. **c)** Basal temperature versus Relief change (R). (For interpretation of the references to color in this figure legend, the reader is referred to the web version of this article.)

the background exhumation rates. The resulting AER slope is concave. For the Gongga batholith, our Pecube modeling shows that the geothermal gradient has been durably perturbed and raised to a high value of ~41.5 °C. However, the time delay between the end of the magmatic pulse at 12 Ma and the onset of rapid exhumation at ~9 Ma, together with the linear AER, suggest that our samples do not record thermal relaxation of the Miocene pulse but a distinct phase of rapid cooling, associated with exhumation.

Our modeling also shows that the cooling rate decreased after ~4 Ma (Fig. 7a). This second phase appears coeval with the early-Pliocene dyke injection (Fig. 4). It is therefore impossible to distinguish the amount of cooling linked to possible thermal relaxation to that resulting from exhumation for that later phase. The inferred exhumation rate of ~0.75 km/Myr is therefore a maximum, as thermal relaxation following dyke emplacement would increase the apparent exhumation rate. Nevertheless, the 4–0 Ma exhumation rate is less than half the rate between ~9 and 4 Ma, showing a decrease of exhumation in this part of the batholith since ~4 Ma (Fig. 8a). We did not infer exhumation rates for the lower part of the Kangding transect, as this area is clearly affected by the early Pliocene re-heating.

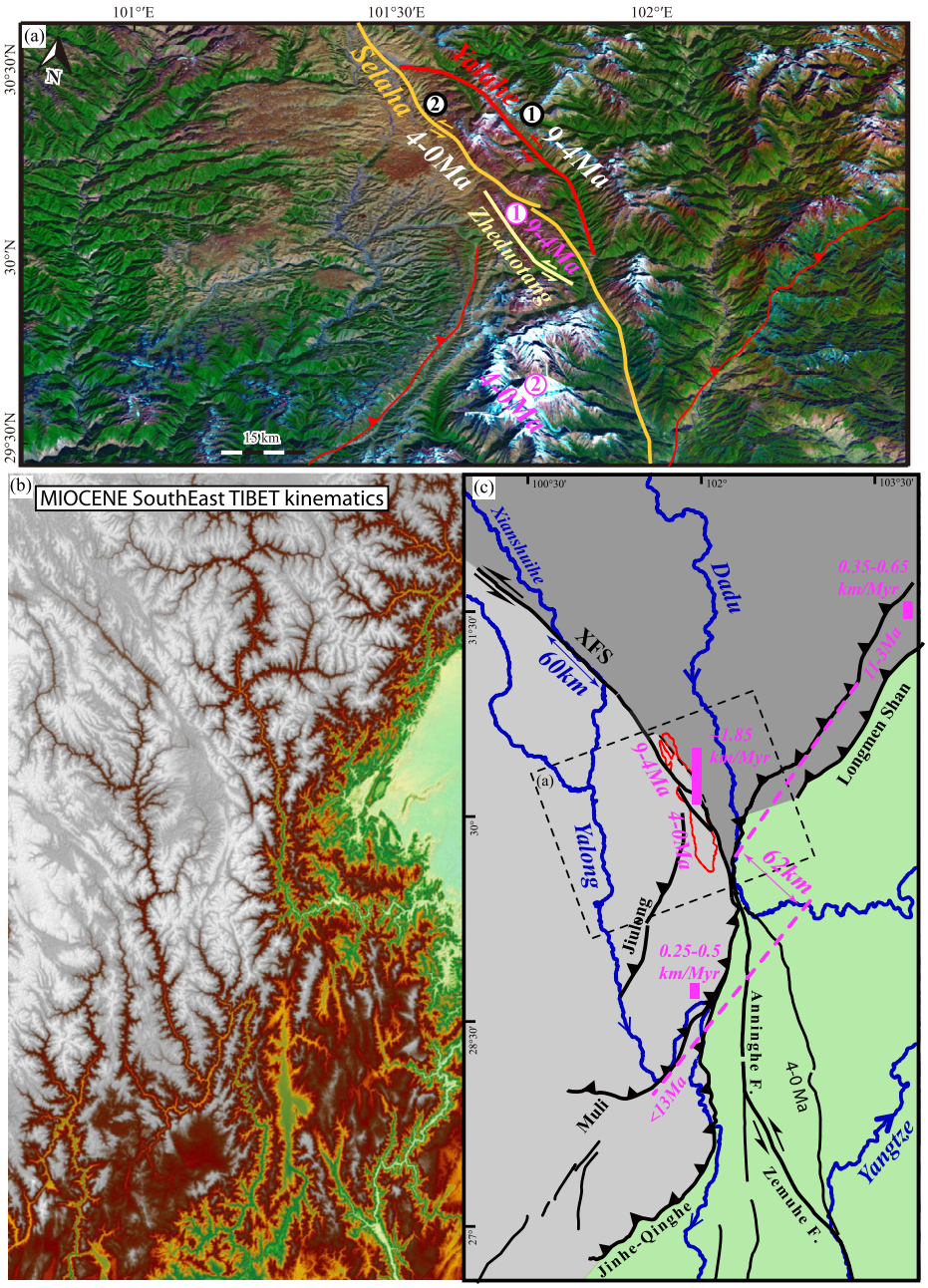

Fig. 8. a) Landsat image draped on Aster DEM of the Gongga batholith region (black dotted frame on c; same frame as Fig. 2) with the Yalahe (red), Selaha (orange) and Zheduotang (yellow) fault segments, and inferred timing of activity (white numbers) with corresponding timing of rapid exhumation (pink numbers). **b)** Topographic map of SE Tibet. **c)** Corresponding sketch showing active faults (black) and rivers (blue), with timing and rate of rapid Miocene exhumation (pink) indicated. (For interpretation of the references to color in this figure legend, the reader is referred to the web version of this article.)

Along the Taizhan transect, our AFT and ZFT ages are between 2 and 4.5 Ma and can be modeled as recording a phase of rapid exhumation with a most probable rate of ~4 km/Myr (considering a most probable thermal gradient of 43 °C/km). This area has been strongly affected by the early Pliocene heating, in agreement with the inferred high thermal gradient, and the calculated exhumation rate is thus a maximum. Following this rapid cooling, our modeling shows a phase of slower exhumation since ~2–3 Ma, at a rate of 0.94 km/Myr.

In the southern part of the Gongga Batholith, south of the Zhedouotang fault, the absence of any published Ar/Ar nor young U/Pb ages render discussion of the possible influence of the early Pliocene magmatic event currently impossible. Recent surface uplift and exhumation rates have not been quantified yet but could be very high, as suggested by the elevation of the Gongga Shan towering at 7756 m, more than 3000 m above the mean plateau elevation (Fig. 3a), and by young FT ages in this area, between 1.2 and 4.2 Ma (Fig. 2c, SM4; Xu and Kamp, 2000). Detrital ^{10}Be cosmogenic data from this southern part of the Gongga Shan also suggest very rapid recent erosion (≥5 mm/yr) (Cook et al., 2016).

6.3. Mio-Pliocene kinematic evolution of the XF

The zone affected by rapid Miocene exhumation is very narrow, about the width of the granite (Fig. 2). It is surrounded by surfaces that are not affected by exhumation, like the Tagong granite south of Bamei town, which shows no significant exhumation since the Cretaceous. This narrow zone of exhumation strongly suggests that it is linked to deformation along the XF.

Along the XF, relatively slow exhumation along the Kanding transect since ∼4 Ma, and along the Taizhan transect since 2–3 Ma, is consistent with the present-day low relief observed between the Selaha and the Zheduotang faults (Fig. 3b). The highest peaks, including the Gongga Shan at more than 7500 m, are located south of the Zheduotang fault (Fig. 3a). Considering that the Selaha and Zheduotang faults are currently the most active segment of the XF and that this segment cuts off a sharp bend in the Yalahe fault, the Gongga Shan massif is located in the present-day sharpest bend of the XF (Fig. 8a). Rapid present-day exhumation occurs in this restraining bend of the XF. In contrast, our results show that between ∼9 and 4 Ma, rapid exhumation occurred north of the Zheduotang fault, along a sharp bend of the Yalahe fault. We suggest that during that period, the Yalahe segment was active, and that the restraining bend was located more to the north (Fig. 8a). Fault transfer at ∼4 Ma from the Yalahe to the Selaha–Zheduotang fault would be coeval with the limited partial-melting event that we documented.

Our results imply ∼9 km of exhumation in the northern part of the Gongga batholith between 9 and 4 Ma, considering our inferred exhumation rate of ∼1.85 km/Myr during this time period. Such significant exhumation is compatible with the formation of high summits, comparable with the Gongga Shan (Fig. 3a). At present, the batholith shows relatively smooth relief at the mean elevation of the plateau (∼4500 m) along the Upper Kangding transect (Fig. 3b), suggesting significant relief reduction since ∼4 Ma. The granite at the surface is strongly affected by frost shattering, with angular blocks covering the surface. Glacial valleys oriented NW-SE have also partly eroded the highest part of the range (Allen et al., 1991). The low relief of the Gongga batholith along the upper Kangding section argues for relief smoothing at high altitude by glacial and periglacial erosion processes (e.g., Egholm et al., 2015; Fig. 8a), as has also been suggested further north (Zhang et al., 2016). Therefore, the Gongga Shan represents a field example confirming that such high-altitude erosion processes are efficient enough to generate smooth in less than 10 Ma the relief of zones that have been affected by strong exhumation.

The total offset documented for the XF in this area from the offset of Xianshuihe River is ∼60 km, matching the offset between thrusts in the Longmen Shan to the east with the Muli thrust to the west (Yan and Lin, 2015; Fig. 8c). Our results suggest that the onset of motion along the XF is contemporaneous with the onset of rapid exhumation recorded along the Kangding transect at ∼9 Ma, linked with transpression in a restraining bend along the fault system. In that case the mean slip rate of the XF would be ∼6.9 mm/yr since 9 Ma. This value corresponds to the upper bound of the Holocene rate, inferred to be 4.6–7.2 mm/yr (Allen et al., 1991), and the lower range of the recent GPS rates (6–15 mm/yr; Liang et al., 2013; Zhang et al., 2013; Zhao et al., 2015).

6.4. Mio-Pliocene kinematic evolution of SE Tibet

Our results confirm that in SE Tibet the youngest FT ages (<15 Ma) are located along large structures as the XF (e.g.; Xu and Kamp, 2000; Wilson and Fowler, 2011), the Litang fault (Zhang et al., 2015) or the Longmen Shan thrust belt (e.g., Wang et al., 2012; Godard et al., 2009) and are related to rapid exhumation, whereas away from these structures FT ages are older and related to very slow exhumation (<0.3 km/Myr) since at least 80 Ma. Our results also show that the exhumation rate documented near the strike-slip XF (∼2 km/Myr) is higher than those documented near regional thrusts or along incised valleys (<1 km/Myr). We interpret this high local exhumation rate to be linked to a restraining bend in the XF. The localization of the most rapid exhumation along both thrust and strike-slip faults is in agreement with a model where localization of deformation in narrow zones prevails over distributed deformation.

In the Longmen Shan, an initial phase of Cenozoic exhumation has been documented during the Oligocene, starting at 30–25 Ma at a rate of ∼0.8 km/Myr (Wang et al., 2012; Tan et al., 2014). Exhumation accelerated again to a rate of ∼0.35 to 0.65 km/Myr at 11–8 Ma (Wang et al., 2012; Godard et al., 2009). Southwest of the XF, in the hanging wall of Muli thrust, exhumation at rates of 0.25 to 0.5 km/Myr started at 13–9 Ma (Clark et al., 2005b). This shows that onset of Miocene thrusting on the Longmen Shan and Muli thrusts was coeval, suggesting that the two systems were continuous before being offset by the XF after 9 Ma.

The Xianshuihe fault system is broadly following a small circle, the pole of which is located in the eastern Himalayan syntaxis (Fig. 1a). Despite strong progress in the modeling of large-scale lithospheric deformation over the last decades, the occurrence of strongly localized strike-slip along structures such as the XFS has not yet been successfully reproduced. Including a viscous component in the rheology of the lithosphere in numerical models does not reproduce such strike-slip faults (e.g. Capitanio et al., 2015) unless they are imposed (Clark et al., 2005a). Therefore, the best model to account for the geometry and kinematics of the XFS remains the conceptual analogy of strike-slip faults with slip-lines in a plastic medium near the corner of a rigid indenter (Tapponnier and Molnar, 1976). The onset of the XFS at ∼9 Ma would then result from a major faults kinematic reorganization after the end of Indochina extrusion at ∼17 Ma and prior to the establishment of the present day fault pattern at ∼7–5 Ma (Zhang et al., 2015).

7. Conclusion

Our data and modeling records a phase of rapid exhumation since ∼9 Ma, at a rate of ∼1.85 km/Myr and slowing down since ∼4 Ma, in the northern Gongga Batholith (Fig. 6). A minor late magmatic pulse occurring during the early Pliocene has overprinted this rapid exhumation phase in some parts of the batholith, which record mostly early Pliocene post-magmatic cooling. Slow exhumation since ∼4 Ma is consistent with the present-day low relief observed north of the Zheduotang fault, whereas the highest peaks are located south of the fault (Fig. 8a). We propose that the Selaha and the Zheduotang faults form a present-day restraining bend in which the high-elevation Gongga Shan massif has been uplifted since the Pliocene. Between ∼9 and 4 Ma, rapid exhumation occurred north of the Zheduotang fault, in the sharp bend of the Yalahe fault, which was active during that period (Fig. 8a). Maximum exhumation between 9 and 4 Ma is ∼9 km, compatible with the formation of high summits comparable to the modern Gongga Shan (Fig. 3a). Such Miocene peaks would have been removed by local glacial and periglacial relief reduction at high elevations in less than 10 Ma (Fig. 3b). Our results show that the onset of left-lateral motion along the XF occurred at ∼9 Ma, with a mean slip rate of ∼7 mm/yr, considering the total offset documented for the XF at 62 km (Fig. 8c), consistent with present-day and Holocene estimates of slip rate.

Acknowledgements

This study has been supported by the National Special Project on the Tibetan Plateau of the Geological Survey of China (Nos. 1212011121261 and 1212010610103), the National Natural Science Foundation of China (No. 41672195), the China Scholarship Council Funds (No. 201206410001) and the Labex OSUG@2020 (Investissements d'avenir – ANR10 LABX56). Campus France PHC XU GUANGQI 2012 N° 27928YC and PHC CAI YUANPEI N° 27968UC (French ministry of foreign affairs) funding is also acknowledged,

as well as support from the SYSTER (INSU-CNRS) program. Elizabeth Hardwick and Mélanie Noury are thanked for sample preparation. Christoph Glotzbach provided the BIC code. We thank Jean Braun for providing the Pecube code and constructive comments on the modeling and Mariane Metois for the analysis of the GPS data.

Appendix A. Supplementary material

Supplementary material related to this article can be found online at http://dx.doi.org/10.1016/j.epsl.2017.02.025.

References

Allen, C.R., Zhuoli, L., Hong, Q., Xueze, W., Huawei, Z., Weishi, H., 1991. Field study of a highly active fault zone: the Xianshuihe fault of southwestern China. Geol. Soc. Am. Bull. 103, 1178–1199. http://dx.doi.org/10.1130/0016-7606(1991)103<1178:fsoaha>2.3.co;2.

Arne, D., Worley, B., Wilson, C., Chen, S.F., Foster, D., Luo, Zhili, Liu, Shugen, Dirks, P.H.G.M., 1997. Differential exhumation in response to episodic thrusting along the eastern margin of the Tibetan Plateau. Tectonophysics 280, 239–256. http://dx.doi.org/10.1016/S0040-1951(97)00040-1.

Bermúdez, M.A., van der Beek, P., Bernet, M., 2011. Asynchronous Miocene–Pliocene exhumation of the central Venezuelan Andes. Geology 39, 139–142. http://dx.doi.org/10.1130/g31582.1.

Bernet, M., 2009. A field-based estimate of the zircon fission-track closure temperature. Chem. Geol. 259, 181–189. http://dx.doi.org/10.1016/j.chemgeo.2008.10.043.

Brandon, M.T., Roden-Tice, M.K., Garver, J.I., 1998. Late Cenozoic exhumation of the Cascadia accretionary wedge in the Olympic Mountains, northwest Washington State. Geol. Soc. Am. Bull. 110, 985–1009. http://dx.doi.org/10.1130/0016-7606(1998)110<0985:lceotc>2.3.co;2.

Braun, J., 2003. Pecube: a new finite-element code to solve the 3D heat transport equation including the effects of a time-varying, finite amplitude surface topography. Comput. Geosci. 29, 787–794. http://dx.doi.org/10.1016/S0098-3004(03)00052-9.

Braun, J., van der Beek, P., Valla, P., Robert, X., Herman, F., Glotzbach, C., Pedersen, V., Perry, C., Simon-Labric, T., Prigent, C., 2012. Quantifying rates of landscape evolution and tectonic processes by thermochronology and numerical modeling of crustal heat transport using PECUBE. Tectonophysics 524–525, 1–28. http://dx.doi.org/10.1016/j.tecto.2011.12.035.

Burchfiel, B.C., Chen, Z., Liu, Y., Royden, L.H., 1995. Tectonics of the Longmen Shan and adjacent regions. Int. Geol. Rev. 37, 661–736.

Capitanio, F.A., Replumaz, A., Riel, N., 2015. Reconciling subduction dynamics during Tethys closure with large-scale Asian tectonics: insights from numerical modeling. Geochem. Geophys. Geosyst. 16, 962–982. http://dx.doi.org/10.1002/2014GC005660.

Chen, W., Zhang, Y., Zhang, Y.Q., Jin, G.S., Wang, Q.L., 2006. Late Cenozoic episodic uplifting in southeastern part of the Tibetan plateau-evidence from Ar–Ar thermochronology. Acta Geol. Sin. 22, 867–872. http://dx.doi.org/10.3969/j.issn.1000-0569.2006.04.010.

Chengdu Institute of Geology and Mineral Resources (CIGMR), 2004. Geological Map of Tibetan Plateau and Its Vicinity. Chengdu Map Press, Chengdu.

Clark, M.K., 2003. Late Cenozoic Uplift of Southeastern Tibet. Massachusetts Institute of Technology, Cambridge (USA).

Clark, M.K., Bush, J.W.M., Royden, L.H., 2005a. Dynamic topography produced by lower crustal flow against rheological strength heterogeneities bordering the Tibetan Plateau. Geophys. J. Int. 162, 575–590. http://dx.doi.org/10.1111/j.1365-246X.2005.02580.x.

Clark, M.K., House, M.A., Royden, L.H., Whipple, K.X., Burchfiel, B.C., Zhang, X., Tang, W., 2005b. Late Cenozoic uplift of southeastern Tibet. Geology 33, 525–528. http://dx.doi.org/10.1130/g21265.1.

Cook, K.L., Hovius, N., Wittmann, H., Heimsath, A.M., Lee, Y.H., 2016. Feedbacks between erosion, climate and uplift in the Gongga Granite on the eastern margin of the Tibetan Plateau. Geophys. Res. Abstr. 18, EGU2016-9373.

de Sigoyer, J., Vanderhaeghe, O., Duchêne, S., Billerot, A., 2014. Generation and emplacement of Triassic granitoids within the Songpan Ganze accretionary-orogenic wedge in a context of slab retreat accommodated by tear faulting, Eastern Tibetan plateau, China. J. Asian Earth Sci. 88, 192–216. http://dx.doi.org/10.1016/j.jseaes.2014.01.010.

Egholm, D.L., Andersen, J.L., Knudsen, M.F., Jansen, J.D., Nielsen, S.B., 2015. The periglacial engine of mountain erosion – Part 2: modelling large-scale landscape evolution. Earth Surf. Dynam. 3, 463–482. http://dx.doi.org/10.5194/esurf-3-463-2015.

Ehlers, T.A., Chaudhri, T., Kumar, S., Fuller, C.W., Willett, S.D., Ketcham, R.A., Brandon, M.T., Belton, D.X., Kohn, B.P., Gleadow, A.J.W., Dunai, T.J., Fu, F.Q., 2005. Computational tools for low-temperature thermochronometer interpretation. Rev. Mineral. Geochem. 58, 589–622. http://dx.doi.org/10.2138/rmg.2005.58.22.

Glotzbach, C., van der Beek, P.A., Spiegel, C., 2011. Episodic exhumation and relief growth in the Mont Blanc massif, Western Alps from numerical modelling of thermochronology data. Earth Planet. Sci. Lett. 304, 417–430. http://dx.doi.org/10.1016/j.epsl.2011.02.020.

Godard, V., Pik, R., Lave, J., Cattin, R., Tibari, B., de Sigoyer, J., Pubellier, M., Zhu, J., 2009. Late Cenozoic evolution of the central Longmen Shan, eastern Tibet: insight from (U–Th)/He thermochronometry. Tectonics 28, TC5009. http://dx.doi.org/10.1029/2008tc002407.

Jiang, G., Wen, Y., Liu, Y., Xu, X., Fang, L., Chen, G., Gong, M., Xu, C., 2015. Joint analysis of the 2014 Kangding, southwest China, earthquake sequence with seismicity relocation and InSAR inversion. Geophys. Res. Lett. 42, 3273–3281. http://dx.doi.org/10.1002/2015GL063750.

Kirby, E., Reiners, P.W., Krol, M.A., Whipple, K.X., Hodges, K.V., Farley, K.A., Tang, W.Q., Chen, Z.L., 2002. Late Cenozoic evolution of the eastern margin of the Tibetan Plateau: inferences from $^{40}Ar/^{39}Ar$ Ar and (U–Th)/He thermochronology. Tectonics 21, 1001. http://dx.doi.org/10.1029/2000tc001246.

Lai, Q.Z., Ding, L., Wang, H.W., Yue, Y.H., Cai, F.L., 2007. Constraining the stepwise migration of the eastern Tibetan Plateau margin by apatite fission track thermochronology. Sci. China, Ser. D Earth Sci. 50, 172–183. http://dx.doi.org/10.1007/s11430-007-2048-7.

Li, H., Zhang, Y., 2013. Zircon U–Pb geochronology of the Konggar granitoid and migmatite: constraints on the Oligo-Miocene tectono-thermal evolution of the Xianshuihe fault zone, East Tibet. Tectonophysics 606, 127–139. http://dx.doi.org/10.1016/j.tecto.2013.07.007.

Li, H., Zhang, Y., Zhang, C., Dong, S., Zhu, F., 2015. Middle Jurassic syn-kinematic magmatism, anatexis and metamorphism in the Zheduo–Gonggar massif, implication for the deformation of the Xianshuihe fault zone, East Tibet. J. Asian Earth Sci. 107, 35–52. http://dx.doi.org/10.1016/j.jseaes.2015.03.038.

Liang, S., Gan, W., Shen, C., Xiao, G., Liu, J., Chen, W., Ding, X., Zhou, D., 2013. Three-dimensional velocity field of present-day crustal motion of the Tibetan Plateau derived from GPS measurements. J. Geophys. Res. 118 (10). http://dx.doi.org/10.1002/2013JB010503.

Liu, S., Wang, Z., Yan, Q., Li, Q., Zhang, D., Wang, J., 2006. Timing, petrogenesis and geodynamic significance of Zheduoshan Granitoids. Acta Geol. Sin. 22, 343–352. http://dx.doi.org/10.3969/j.issn.1000-0569.2006.02.008.

Liu-Zeng, J., Tapponnier, P., Gaudemer, Y., Ding, L., 2008. Quantifying landscape differences across the Tibetan plateau: implications for topographic relief evolution. J. Geophys. Res., Earth Surf. 113, F04018. http://dx.doi.org/10.1029/2007jf000897.

Ouimet, W., Whipple, K., Royden, L., Reiners, P., Hodges, K., Pringle, M., 2010. Regional incision of the eastern margin of the Tibetan Plateau. Lithosphere 2, 50–63. http://dx.doi.org/10.1130/l57.1.

Reid, A.J., Fowler, A.P., Phillips, D., Wilson, C.J.L., 2005. Thermochronology of the Yidun Arc, central eastern Tibetan Plateau: constraints from $^{40}Ar/^{39}Ar$ K-feldspar and apatite fission track data. J. Asian Earth Sci. 25, 915–935. http://dx.doi.org/10.1016/j.jseaes.2004.09.002.

Reiners, P.W., Brandon, M.T., 2006. Using thermochronology to understand orogenic erosion. Annu. Rev. Earth Planet. Sci. 34, 419–466. http://dx.doi.org/10.1146/annurev.earth.34.031405.125202.

Roger, F., Calassou, S., Lancelot, J., Malavieille, J., Mattauer, M., Xu, Z.Q., Hao, Z.W., Hou, L.W., 1995. Miocene emplacement and deformation of the Konggashan granite (Xianshui-he fault zone, West Sichuan, China): geodynamic implications. Earth Planet. Sci. Lett. 130, 201–216. http://dx.doi.org/10.1016/0012-821x(94)00252-t.

Searle, M.P., Roberts, N.M.W., Chung, S.-L., Lee, Y.-H., Cook, K.L., Elliott, J.R., Weller, O.M., St-Onge, M.R., Xu, X.-W., Tan, X.-B., Li, K., 2016. Age and anatomy of the Gongga Shan batholith, eastern Tibetan Plateau, and its relationship to the active Xianshui-he fault. Geosphere. http://dx.doi.org/10.1130/ges01244.1.

Simon-Labric, T., 2011. Cooling, Exhumation and Topographic Evolution in Continental Magmatic Arcs: An Integrated Thermochronological and Numerical Modelling Approach: Example from North Cascades (U.S.A.) and the Motagua Fault Zone (Guatemala). PhD Earth Sciences. Université Grenoble-Alpes. <NNT: 2011GRENU010>, <tel-00591413>.

Tan, X.B., Lee, Y.H., Chen, W.Y., Cook, K.L., Xu, X.W., 2014. Exhumation history and faulting activity of the southern segment of the Longmen Shan, eastern Tibet. J. Asian Earth Sci. 81, 91–104.

Tapponnier, P., Molnar, P., 1976. Slip-line field-theory and large-scale continental tectonics. Nature 264, 319–324.

Tapponnier, P., Xu, Z.Q., Roger, F., Meyer, B., Arnaud, N., Wittlinger, G., Yang, J.S., 2001. Oblique stepwise rise and growth of the Tibet plateau. Science 294, 1671–1677. http://dx.doi.org/10.1126/science.105978.

Tian, Y., Kohn, B.P., Gleadow, A.J.W., Hu, S., 2014. A thermochronological perspective on the morphotectonic evolution of the southeastern Tibetan Plateau. J. Geophys. Res., Solid Earth 119, 676–698. http://dx.doi.org/10.1002/2013JB010429.

Valla, P.G., Herman, F., van der Beek, P.A., Braun, J., 2010. Inversion of thermochronological age-elevation profiles to extract independent estimates of denudation and relief history — I: theory and conceptual model. Earth Planet. Sci. Lett. 295, 511–522. http://dx.doi.org/10.1016/j.epsl.2010.04.033.

Wallis, S., Tsujimori, T., Aoya, M., Kawakami, T., Terada, K., Suzuki, K., Hyodo, H., 2003. Cenozoic and Mesozoic metamorphism in the Longmenshan orogen: im-

plications for geodynamic models of eastern Tibet. Geology 31, 745–748. http://dx.doi.org/10.1130/g19562.1.

Wang, C.-Y., Lou, H., Silver, P.G., Zhu, L., Chang, L., 2010. Crustal structure variation along 30°N in the eastern Tibetan Plateau and its tectonic implications. Earth Planet. Sci. Lett. 289, 367–376. http://dx.doi.org/10.1016/j.epsl.2009.11.026.

Wang, E., Kirby, E., Furlong, K.P., van Soest, M., Xu, G., Shi, X., Kamp, P.J.J., Hodges, K.V., 2012. Two-phase growth of high topography in eastern Tibet during the Cenozoic. Nat. Geosci. 5, 640–645. http://dx.doi.org/10.1038/ngeo1538.

Wang, S.F., Fang, X.M., Zheng, D.W., Wang, E.C., 2009. Initiation of slip along the Xianshuihe fault zone, eastern Tibet, constrained by K/Ar and fission-track ages. Int. Geol. Rev. 51, 1121–1131. http://dx.doi.org/10.1080/00206810902945132.

Wilson, C.J.L., Fowler, A.P., 2011. Denudational response to surface uplift in east Tibet: evidence from apatite fission-track thermochronology. Geol. Soc. Am. Bull. 123, 1966–1987. http://dx.doi.org/10.1130/b30331.1.

Xu, G.Q., Kamp, P.J.J., 2000. Tectonics and denudation adjacent to the Xianshuihe Fault, eastern Tibetan Plateau: constraints from fission track thermochronology. J. Geophys. Res., Solid Earth 105, 19231–19251. http://dx.doi.org/10.1029/2000jb900159.

Xu, T.-D., 2009. Petrographical features of the Zheduoshan Granite Pluton in Kangding and their tectonic implication. Acta Geol. Sichuan 29, 58–64. http://dx.doi.org/10.3969/j.issn.1006-0995.2009.z1.010.

Yan, B., Lin, A., 2015. Systematic deflection and offset of the Yangtze River drainage system along the strike-slip Ganzi–Yushu–Xianshuihe Fault Zone, Tibetan Plateau. J. Geodyn. 87, 13–25. http://dx.doi.org/10.1016/j.jog.2015.03.002.

Zhang, H., Oskin, M.E., Liu-Zeng, J., Zhang, P., Reiners, P.W., Xiao, P., 2016. Pulsed exhumation of interior eastern Tibet: implications for relief generation mechanisms and the origin of high-elevation planation surfaces. Earth Planet. Sci. Lett. 449, 176–185. http://dx.doi.org/10.1016/j.epsl.2016.05.048.

Zhang, Y.Q., Chen, W., Yang, N., 2004. $^{40}Ar/^{39}Ar$ dating of shear deformation of the Xianshuihe fault zone in west Sichuan and its tectonic significance. Sci. China, Ser. D Earth Sci. 47, 794–803. http://dx.doi.org/10.1360/03yd0509.

Zhang, Y.-Z., Replumaz, A., Wang, G.-C., Leloup, P.H., Gautheron, C., Bernet, M., van der Beek, P., Paquette, J.L., Wang, A., Zhang, K.-X., Chevalier, M.-L., Li, H.-B., 2015. Timing and rate of exhumation along the Litang fault system, implication for fault reorganization in Southeast Tibet. Tectonics 34, 1219–1243. http://dx.doi.org/10.1002/2014TC003671.

Zhang, Z., McCaffrey, R., Zhang, P., 2013. Relative motion across the eastern Tibetan plateau: contributions from faulting, internal strain and rotation rates. Tectonophysics 584, 240–256. http://dx.doi.org/10.1016/j.tecto.2012.08.006.

Zhao, B., Huang, Y., Zhang, C., Wang, W., Tan, K., Du, R., 2015. Crustal deformation on the Chinese mainland during 1998–2014 based on GPS data. Geod. Geodyn. 6, 7–15. http://dx.doi.org/10.1016/j.geog.2014.12.006.